Experimental Comparison of Tracking Algorithms in the Presence of Aircraft Boundary-Layer Distortions for an Emulated Free-Space Laser Communications Link

Ross A. Conrad[1,*], Robert J. Murphy[2], Timothy H. Williams[2], William E. Wilcox[2], Steven Michael[2], and Jeffrey M. Roth[2,*]

[1] *Department of Aeronautics and Astronautics, Massachusetts Institute of Technology,*
77 Massachusetts Avenue, 33-207, Cambridge, MA 02139, USA

[2] *MIT Lincoln Laboratory,*
244 Wood Street, Lexington, MA 02420, USA

[*] *Corresponding authors:* raconrad@gmail.com, jroth@ll.mit.edu

We report on experiments comparing different focal plane array (FPA) tracking algorithms for emulated laser communications links between an aircraft and spacecraft. The links include look-angle-dependent phase disturbances caused by boundary-layer turbulence replicated using a deformable mirror. Impairments from platform jitter, atmospheric scintillation, and propagation delay are also included. We study a hyper-hemispherical dome geometry that provides a large field-of-regard, but generates boundary-layer turbulence. Results from experiments comparing peak and centroid FPA tracking algorithms in various environments show that power delivered to the optical fiber varies with algorithm and look-angle. An improvement in steady-state fiber-coupled power of up to 1.0 dB can be achieved through appropriate choice of algorithm. In a real system, this advantage could be realized by implementing a tracking processor that dynamically changes its tracking algorithm depending on look angle and other parameters correlated to boundary-layer turbulence.

OCIS codes: 010.1330 (Atmospheric turbulence), 060.2605 (Free-space optical communication).

1. Introduction

Free-space laser communication (lasercom) utilizes a high optical carrier frequency to transport data. As a result, lasercom supports data rates in the 2.5- to 40-Gb/s range, surpassing the rates of current radio-frequency (RF) systems. Furthermore, short lasercom wavelengths diffract less, providing high antenna gain for relatively small apertures compared to the RF domain. These advantages make airborne lasercom attractive for providing mobile, edge users with rapidly deployable, high-data-rate connectivity into space and terrestrial backbone networks.

While the use of short lasercom wavelengths (typically in the 1- to 1.5-μm band)

provides high antenna gain and high carrier frequency, the narrow beamwidths lead to pointing and tracking challenges for mobile platforms. Lasercom systems typically require an optical tracking system to stabilize against local platform jitter by using the received optical beam as a reference. In most cases, this technique requires both ends of the link to simultaneously track each other. The initial acquisition sequence involves steps to illuminate the remote terminal given uncertainty in its precise location. The acquisition must also function in the presence of local platform jitter. Furthermore, tracking systems for long-distance lasercom links must also accommodate propagation latencies of up to 0.25 sec for geosynchronous-earth-orbit (GEO) ranges.

Air-to-space lasercom links face a unique set of challenges including the above effects, and in addition atmospheric fading and boundary-layer phase distortions. Atmospheric variations produce scintillation of the optical signal in the far-field at the remote terminal, leading to fades and dropouts through which the pointing, tracking, and communication systems must operate [1]. Boundary-layer phase distortions result from uneven airflow around the fuselage of an aircraft. The boundary-layer effects depend heavily on the interface geometry between the terminal and the aircraft exterior. Terminals with protruding turrets may in principle provide a large field-of-regard, but disruptions to laminar airflow around them may reduce operability. Conversely, a flat window may not generate boundary-layer distortions, but offers a more restricted field-of-regard.

At optical wavelengths, airflow non-uniformities from boundary-layer effects can distort an optical beam's phase front. The phase distortions Fourier-transform to beam intensity profile variations in the focal plane, where the optical tracker usually resides. The beam distortions begin as tip and tilt (jitter) at the tracking sensor. Stronger boundary-layer turbulence can produce higher-order distortions and eventually break-up a single-mode beam into multiple peaks. Tracking a beam in the presence of boundary-layer distortions becomes more difficult for these reasons. Fur-

thermore, inertial sensing cannot remove boundary-layer-induced tilt. While adaptive optics could be used to mitigate boundary-layer impairments, that approach requires added resources and complexity. This paper instead focuses on addressing the varying degrees of boundary-layer phase distortions through appropriate choice of tracking algorithm.

In this work, the impact of boundary-layer phase distortions was investigated in a laboratory testbed that provides a realistic emulation of lasercom links between airborne and space-based platforms. The testbed contains hardware and software-controlled, full-duplex, tracking systems representing aircraft and spacecraft terminals. The impairments applied to the signals include propagation delay, platform jitter, atmospheric scintillation, and boundary-layer phase distortions. Fig. 1 shows the testbed's functionality. This paper describes several testbed experiments on tracking algorithms and discusses the results.

2. Laboratory Testbed Capability

The laboratory testbed contains two full-duplex tracking terminals. Both terminals are equipped with a focal-plane array (FPA) tracking camera used as a tracking sensor, and a quadrant-cell detector (QC) used as a narrow field-of-view (FOV) fine-tracking sensor. The QC performs higher-rate tracking than the FPA, yet can only exercise a median tracking algorithm, while the FPA can perform more sophisticated processing. The tracking bandwidth of the FPA could be extended through use of inertial sensing to stabilize out high-frequency local platform jitter. The FPA sensor is a commercially available Phoenix InGaAs camera, made by FLIR Systems. This camera has a 320×256 pixel format that images at 345 frames per second (fps) in full-window mode [2]. In the laboratory testbed, the tracker FOV requirements permit operating the FPA in a sub-windowed format of 64×128 pixels that supports a higher frame rate of 2.367 kilo-frames per second (kfps). Given the Nyquist sampling criteria,

the FPA can view disturbances out to 1.183 kHz.

Closed-loop tracking on each terminal is carried out using a mechanical fast-steering mirror (FSM). A second FSM functions as a point-ahead mirror that offsets transmit and receive beams to accommodate relative transverse motion between platforms [3]. For example, an air-to-GEO link requires a maximum point-ahead angle of approximately a 20 μrad. This mirror also performs a spiral scan of the transmit beam during the initial acquisition sequence. Fiber launch assemblies are used to transmit the signals into free space and couple the receive beams into fiber.

Fine-tracking of the beam into an optical fiber is a fundamental prerequisite for high-rate-communication signaling. Therefore, the terminal hardware does not include high-date-rate modems since we do not directly investigate communications performance in this work. Rather, this work focuses on the performance of pointing, acquisition, and tracking required to set up a link, maintain it, and ultimately support communications. The communication system can overcome channel-induced power fluctuations not corrected by the tracking system through the use of forward-error-correction and interleaving techniques [3].

Careful emulation of the environment allows for a full range of programmable disturbances to be applied to the optical signals. Far-field simulators using spatial filters constructed of over-filled, fiber-coupling optics emulate the propagation of the beam into the far field. Tests discussed in this paper use fixed aperture diameters of 38 mm (1.5 in) for the aircraft and 305 mm (12 in) for the spacecraft. Over GEO ranges, a beam expands to diameters large compared to the receive telescope diameter. The far-field simulators allow each terminal to deliver a flat irradiance profile to the remote terminal's aperture, permitting the terminals to reside in close proximity, rather than the 36,000 to 41,000-km range for an actual air-to-GEO link. Once in fiber, the channel emulator modulates atmospheric scintillation effects onto the signals using lithium-niobate, electro-optic intensity modulators. The atmospheric

scintillation is generated using a rigorous, wave-optics beam propagation model that includes Kolmogrov phase screens to produce time series of power fading for different link geometries [1]. The channel emulator also applies propagation delays using an optical-to-electrical converter, an electronic real-time buffer, and a regenerator laser. Independent platform jitter is applied to both terminals using a disturbance mirror. The jitter for each terminal can represent the vibration spectrum for arbitrary platforms. Future testbed enhancements could include additional atmospheric channel effects, for example jitter-dependent scintillation or variation between uplink and downlink path effects [4].

An aircraft's boundary-layer turbulence is emulated in the laboratory using a micro-electro-mechanical system deformable mirror (MEMS DM). Density variations present in boundary-layer turbulence can impart a nonuniform phase shift to the beam. In the testbed, this is accomplished using a MEMS DM, which produces optical path difference (OPD) across the beam. We drive this boundary-layer emulator using computational fluid dynamics (CFD) simulations. The simulations model a hyper-hemispherical-shaped turret on a cylindrical airframe flying at a 29,000-foot (29 kft) altitude and Mach-0.7 airspeed. A snapshot of the flow-field generated by the simulations is shown in Fig. 2. This hyper-hemisphere geometry has the advantage of a large field-of-regard when boundary-layer effects are negligible (e.g., at high altitude), but can produce strong boundary-layer conditions for many conditions. At forward directions near 45° elevation a super-sonic shock wave forms, and at backwards directions turbulent wakes and eddies develop. From the CFD simulations, a time series of OPD maps for a given aperture size and look angle is generated. These effects are replicated across the MEMS DM surface [5]. Future work may utilize CFD data for different turret geometries.

3. Experimental Testing

The behavior of boundary-layer disturbances varies with look angle, so a thorough understanding of the impact on tracking performance requires analyzing multiple look angles. Look angles in the experiments were chosen as combinations of 0°, 45°, 90°, 135°, and 180° azimuths, and 10°, 20°, 45°, and 90° elevations. These combinations produce 16 unique look angles (denoted throughout as Az/El) covering half of the full, hemispherical field-of-regard. Horizontally-symmetric look angles should perform similarly based on horizontal symmetry of the hyper-hemispherical geometry. The CFD data is not identical for horizontally symmetric view angles, but the characteristics are very similar. This approximation helps to keep the number of experiments manageable. We define the look angles with respect to the aircraft per Fig. 3. The location of the optical terminal specifies the origin.

Two FPA tracking algorithms were tested at each of the 16 look angles: a peak tracking algorithm, which uses the brightest pixel for pointing, and a centroid tracking algorithm, which calculates the beam's center of mass on the FPA. When the boundary layer causes beam Strehl reduction or beam break-up into multiple peaks, these algorithms provide different results. We also varied the tracking state machine regression rates, which determine how long the sensor attempts to continue tracking when a power dropout occurs. For simplicity, we only varied the aircraft and spacecraft terminal parameters together. Therefore, the experiments use identical configurations for the tracking algorithms and regression rates on the aircraft and spacecraft terminals. We did not investigate asymmetric configurations, though such cases could show additional improvements. These choices for the trade space of view angles and tracker configurations led to a total of 64 experiments to cover the boundary-layer trade space. These testbed experiments include platform jitter, atmospheric fading, far-field propagation, round-trip delay, and the boundary-layer distortions.

The laboratory testbed includes a telemetry system that samples and archives data

on all the sensors and actuators in the facility for data post-processing. After completing the experiments, telemetry data was retrieved to compute mean and standard deviation for two periods during each experiment when the link was active. The first period includes the applied disturbances, and is followed by a second disturbance-free period for reference. This method allowed differences in performance between the tracking configurations to be more easily identified using statistical analysis.

4. Parameters of Interest

We now discuss the figures of merit used to assess performance of each tracking configuration. The primary telemetry parameters chosen for monitoring at each terminal include power density on aperture, FPA peak-pixel power, and fiber-coupled power. Power density on aperture (units: $\mathrm{dB}\left[\frac{\mathrm{W}}{\mathrm{m}^2}\right]$) is a measure of the radiance onto the terminal aperture and is useful for looking at the effects of atmospheric fading. FPA peak-pixel power (units: $\mathrm{dB}\left[\frac{\mathrm{W}}{\mathrm{m}^2}\right]$) is the intensity of the brightest pixel on the FPA, which indicates the optical beam's Strehl ratio. Reduction in on-axis intensity from Strehl decreases power to the tracking system and can result from boundary-layer-induced wavefront distortions. Finally, fiber-coupled power (units: dBm) is the power coupled into the diffraction-limited, single-mode optical fiber for use by the communications receiver. Strehl reduction caused by boundary-layer distortions also impacts fiber-coupling efficiency. To compare tracking algorithms, we monitor all three parameters, with fiber power given the most consideration since it provides a joint indication of communications and tracking performance.

The power-level parameters vary in magnitude during an experiment due to the platform disturbances and the acquisition sequence. Each acquisition begins with the aircraft terminal spiral-scanning the uncertainty region of the spacecraft. Once the terminals have located each other they close-loop track on the other's communication beam. Fig. 4 plots the power-level parameters versus time for a typical link acquisi-

tion. At 15 sec, the aircraft terminal (center plot) begins scanning for the spacecraft terminal (top plot). At 37 sec, the terminals locate each other, respond accordingly, and establish a stable link. Power levels rise but still fluctuate at this point due to disturbances in the channel. Mean power levels are recorded to evaluate tracking performance for the applied disturbances. During 58–62 sec, the disturbances are removed and power levels stabilize, allowing collection of reference power levels. Occasional spikes in the data of Fig. 4 result from system noises and are avoided for mean and standard deviation calculations.

The right axes in the top two graphs of Fig. 4 also specify the terminal state number versus time, corresponding to each terminal's mode of operation. The lower state numbers (0 to 4) refer to initial pointing and acquisition steps, while the higher state numbers ($\geq$5) correspond to optical tracking — the focus of this paper. States 5 and 6 for the spacecraft and aircraft terminals, respectively, refer to FPA tracking, suitable for large-angle disturbances and limited rejection bandwidth. States 6 and 7 for the spacecraft and aircraft terminals, respectively, refer to fine tracking using a quadrant-cell detector, suitable for small angular disturbances and high-bandwidth disturbance rejection. In all cases except the light impairments at 0°/45° (azimuth/elevation) and ±45°/45°, FPA tracking was used since the dropouts were too deep to accommodate tracking using the QC. For that reason, these three look angles tend to show small performance differences between the two FPA tracking algorithms.

5. Format of the Experimental Results

To summarize the large amount of experimental data gathered from the experiments, we show the results graphically using "bullseye" plots defined in Fig. 5. Each region represents an azimuth and elevation pair (look angle). Azimuth is measured relative to the nose of the aircraft as shown in Fig. 3. In the plots, azimuth increases in a clockwise direction with 0° at the top of the page. Elevation angle increases towards

the center of the plot, with the center-most circle representing the zenith angle. (One can visualize the plot as the inside of a segmented umbrella spread overhead.) The aggressive conditions at 90°/10°, 180°/10°, and 270°/10° look angles inhibited stable measurements of link performance. We indicate those cases by an "X" (and colored gray in the online version) in the corresponding regions of the "bullseye" plots. In general, the lower the elevation angle, the heavier the fading due to the greater amount of atmosphere traversed [1].

6. Experimental Results

6.A. Fiber-Coupled Power

The difference between peak and centroid tracking algorithms for power to the optical fiber (in dB) are presented in Figs. 6.a and 6.b for the spacecraft and aircraft terminals, respectively. These graphs are based on mean power collected over stable periods of the link. They do not take into account differences in link attributes such as acquisition time or sporadic regression of the link due to atmospheric fading or boundary-layer distortions. Fig. 6.a demonstrates that centroid algorithms outperform peak algorithms in all but one case on the spacecraft terminal; peak-tracking algorithms perform slightly better at the 180°/20° look angle.

The aircraft terminal shows slightly different performance in Fig. 6.b. While the majority of look angles show a preference for centroid tracking algorithms, peak tracking performed better in some cases. Peak tracking proved best at forward, 45° elevation angles, and at rear-facing cases of ±135°/20° and 180°/20°.

In free-space laser communications, the tracking problem is a coupled, two-body problem. The ability to deliver power to the remote terminal depends strongly on the degree to which local platform jitter is rejected, which in turn depends on the stability of the beam received from the remote terminal. Ideally, maximizing received power should also maximize power delivered to the remote terminal. However, data for some

look angles in Fig. 6 show that a discrepancy can occur between these two figures of merit, meaning optimizing received power does not always optimize power at the remote terminal. (Note that we only performed experiments with symmetric algorithm configurations. Indications from the data that asymmetric algorithm configurations might simultaneously increase both figures of merit requires further verification.)

For air-to-space links, the position of boundary-layer distortions leads to an asymmetric link impairment. The aircraft experiences boundary-layer distortions in its aperture plane (the near field), while the spacecraft sees the far-field profile of the distorted beam. To first order, the image in a receiver focal plane approximately represents the far-field image pattern, meaning the two figures of merit should track toother.

However, this assumption about the focal plane and far field images is not always valid. For example, if there is non-identical beam truncation on the transmit and receive paths, then the transmitted and received mode-field patterns may differ. There may also be differences between the platform-jitter-rejection performance of each terminal. In addition, the scintillation effects experienced by each terminal's tracking system occur independently and in a decorrelated manner. As a result of these realities, discrepancies can occur such that an algorithm that optimizes the received power does not optimize the power delivered to the remote terminal.

In such cases where the same look angle shows different optimal algorithms for the spacecraft and aircraft, choosing a single algorithm for both terminals will only benefit one terminal. This might be appropriate if one terminal (most likely the spacecraft) has more stringent size, weight, and power restrictions. In that case, a system-level design would choose the optimal algorithm for the more constrained terminal. On the other hand, future investigation of asymmetric algorithm configurations would also indicate whether operating each terminal with a unique algorithm would simultaneously benefit both terminals over all look angles.

6.B. FPA Peak-Pixel Power

The differences between the two algorithms for FPA peak-pixel power are shown in Fig. 7. The differences for peak-pixel power are typically smaller than for fiber power. However, the experiments reveal that for the spacecraft, centroid tracking outperforms peak tracking at all operable look angles. For the aircraft terminal, differences between the algorithms were small ($\leq$0.14 dB) over all look angles.

During light disturbances at forward look angles, centroid tracking exhibits only a small advantage over peak tracking on the spacecraft terminal. At 90°/20° and 180°/20°, the differences are larger in favor of centroid tracking. It is difficult to draw conclusions about the aircraft terminal due to the smaller differences. In some cases, an algorithm that performed optimally for one terminal performed sub-optimally for the other terminal. At those look angles, one might choose the algorithm that provides the biggest gain for the spacecraft and only a small penalty for the aircraft. These results further motivate testing of asymmetric algorithm configurations.

6.C. Power Density on Aperture

Fig. 8 provides results for power density on aperture, again showing that centroid tracking is generally preferable. However, this parameter had three occurrences of peak tracking appreciably outperforming centroid tracking on the spacecraft terminal. The most notable case of 180°/20° shows approximately a 1 dB gain from peak tracking. The aircraft terminal power density, as with FPA peak-pixel power, shows smaller differences between peak and centroid tracking.

7. Statistical Analysis

Statistical analysis of the results was performed to make more definitive statements about the experimental observations. For these experiments, the mean and standard deviation of the power levels were calculated from data sampled at 500 Hz for 5 sec.

Using this data, centroid and peak populations could then be compared using a Z test. The test statistic is calculated by Equation 1 with substitution of the experimental means ($\bar{x}$, $\bar{y}$), standard deviations (σ_1, σ_2), and sample sizes (m, n). To use this test, both populations must be approximately normally distributed, independent of each other, and randomly sampled [6], which our data satisfies.

$$Z = \frac{\bar{x} - \bar{y}}{\sqrt{\frac{\sigma_1^2}{m} + \frac{\sigma_2^2}{n}}} \tag{1}$$

To determine whether the two algorithms are in fact different, a two-tailed 99%-confidence interval was created. This corresponds to a Z value that satisfies $|Z| > 2.58$. When exceeding that value, a 99% confidence exists that the algorithm performance differs. Table 1 contains the calculated Z scores between peak and centroid tracking. Positive values signify that centroid tracking performs better, while negative values indicate that peak tracking performs better. Increasing magnitude of the Z score represents increasing confidence.

An examination of Table 1 shows that many Z scores exceed the 99% threshold of $\pm$ 2.58. For the spacecraft terminal's fiber power, all but one look angle prefer centroid tracking at a statistically significant level. For the aircraft terminal fiber-coupled power, it can be seen that the results are more mixed. The other parameters can be similarly examined.

8. FPA Tracking Bandwidth Experiment

The results indicate that the differences between peak and centroid FPA tracking algorithms, in terms of mean power, can be up to 1 dB. One might expect a larger improvement since the two algorithms behave very differently. For example, a fluctuating bi-modal distribution on the FPA, resulting from strong boundary-layer distortions, causes the peak algorithm to hop discontinuously from one peak to another. The corresponding motion would mimic the FSM servo's step response, producing poor

tracking performance. On the other hand, centroid tracking, by intuition a center-of-mass calculation, might position the tracker at a null of the beam in the case of a multi-modal distribution. Such a scenario would deliver insufficient power to the remote terminal's aperture and into the local terminal's receive fiber.

We suspect that the less-dramatic improvement observed results from the limited tracking bandwidth available with the FPA. The FPA and FSM have very high respective frame rates and bandwidths. However, closing the tracking loop typically reduces the bandwidth by ten-fold, leading to a closed-loop bandwidth of approximately 100 Hz.

To see if the limited bandwidth of FPA tracking affects the FPA error signals, an additional experiment was conducted with boundary-layer disturbances only. A look angle of $90°/20°$ was chosen because of the bi-modal beam shape it generated, and because this case should produce different behavior between peak and centroid algorithms. For each algorithm, data was collected from the camera processor with the tracking system running open-loop and not providing feedback control to the FSM. The FPA error signals for each were compared and plotted as shown in Fig. 9. As expected, the peak algorithm has discrete jumps on the order of the camera pixel resolution (1 pixel $\equiv \frac{1}{2}$(beamwidth) $= \frac{\lambda}{2D} \simeq 20$ μrad), while the centroid algorithm varies more smoothly.

Next, we processed the signals through a 100-Hz, low-pass filter to observe the effects from the reduction in bandwidth that occurs when closed-loop tracking. These results, labeled filtered, are also shown in Fig. 9. Distinctions between peak and centroid become less distinguished after filtering. This may explain why peak and centroid perform similarly, even at challenging look angles when the algorithm behaviors differ. With a higher-bandwidth control loop on the FPA tracker, more significant differences between algorithms would be expected.

9. Analysis and Conclusions

Light disturbances from the combination of boundary layer, fading at 45° elevation, and jitter cause manageable problems for the tracking system, and observed performance differences generally fall in the 0.25-dB range. This leads to the conclusion that peak and centroid perform comparably under light disturbances. Moderate fading (20° elevation) generally favors centroid tracking, and the experiments show improvements of up to 1 dB over peak tracking. Heavy fading (10° elevation) combined with boundary-layer disturbances produces very difficult tracking environments for the hyper-hemispherical turret studied. Most of these view angles also preferred centroid tracking. The 10° elevation angle at 29 kft is particularly challenging for lasercom due to strong atmospheric fading. The 90° and 180° azimuth cases at this elevation angle were so turbulent that a stable link did not occur for this turret geometry, altitude, and airspeed. The 0° azimuth case was marginal and approaches the system's limits, mainly due to the extended atmospheric fading time scales that produce longer dropout periods through which the tracker must operate [7].

The best performing algorithm was generally consistent across the three parameters measured. However, as the three parameters are sensitive to different impairments, some look angles shows variation in algorithm performance across the parameters of interest. For example, the spacecraft power levels at 10° elevation angles and the zenith (0°/90°look angle) show different optimal algorithms. Such look angles require additional experiments to further quantify the improvements.

For some look angles, the optimal algorithm for the spacecraft differs from the optimal algorithm for the aircraft, meaning maximizing power received does not always maximize power delivered to the remote terminal. This effect can result from system realities such as the far-field beam pattern differing from the focal-plane pattern, and differences in each terminal's dynamics. These observations indicate that asymmetric configurations of tracking algorithms should be studied. For future work, we also plan

to investigate other tracking algorithms and window interface geometries to better understand how to mitigate the boundary-layer impact without adaptive optics.

10. Summary

These experiments show that for the hyper-hemispherical dome centroid tracking delivers more power to the remote terminal than peak tracking in most conditions. In mild boundary-layer turbulence and atmospheric fading, both methods performed similarly, especially in cases achieving QC tracking. In more turbulent environments, centroid tracking algorithms tend to outperform peak tracking algorithms, as we showed in detailed case-by-base comparisons. Many of the differences between peak and centroid tracking are statistically significant, and might be even more pronounced with a higher-bandwidth FPA control loop that more closely follows the boundary-layer dynamics.

Results indicate that the improvement is not always obtained at both terminals due to the asymmetries of a real system. Therefore, optimizing received power does not always optimize power delivered to the remote terminal. On the order of a few tenths of a dB, these differences are small but could become more significant if the tracker bandwidth limitations discussed in Section 8 were resolved.

Nevertheless, the choice of algorithm can offer a definitive improvement against boundary-layer impairments at certain look angles. This principal could reasonably be implemented in a tracking processor that dynamically changes its tracking algorithm depending on look angle. Adaptive optics might be able to provide further benefit, if the additional hardware and complexity could be accommodated, and if it provided sufficient bandwidth. In the experiments performed here using only algorithms, some of the improvements observed from choosing between centroid- and peak-tracking algorithms approach 1.0 dB. For fiber-coupled power intended for a high-rate communications receiver, this improvement is a significant enhancement as

most free-space optical communication links operate in the photon-starved regime with narrow margins.

Acknowledgments

This work was sponsored by the Department of the Air Force under Air Force Contract FA8721-05-C-0002. Opinions, interpretations, conclusions, and recommendations are those of the authors and are not necessarily endorsed by the United States Government.

References

1. R. Parenti, R.J. Sasiela, L.C. Andrews, and R.L. Phillips. Modeling the PDF for the irradiance of an uplink beam in the presence of beam wander. *Proc. SPIE 6215*, pages 621508.1–13, 2006.
2. FLIR Systems. ThermaCAM Phoenix, Product Brochure, 2004.
3. Stephen G. Lambert and William L. Casey. *Laser Communications in Space*, chapter 3. Artech House, Norwood, MA, 1995.
4. M. Belen'kii, K. Hughes, T. Brinkley, and J. Oldenettel. Residual Turbulent Scintillation Effect and Impact of Turbulence on Fourier Telescopy System. *Proc. SPIE 5160*, pages 56–67, 2004.
5. R.A. Conrad, W.E. Wilcox, T.H. Williams, S. Michael and J.M. Roth, MIT Lincoln Laboratory, 244 Wood Street, Lexington, MA 02420, USA. Authors are preparing a manuscript to be called "Emulation of Boundary-Layer Turbulence on Aircraft Laser Communication Terminals using a Deformable Mirror". Corresponding author email: *jroth@ll.mit.edu*.
6. J. Devore. *Probability and Statistics for Engineering and the Sciences*, pages 361–71 (sec. 9.1: z Tests and Confidence Intervals for a Difference Between Two Population Means). Thomson-Brooks/Cole, 2004.

7. Ross Aaron Conrad. Impact of the Boundary Layer on Pointing and Tracking in Airborne Free-Space Laser Communication Links. Master's Dissertation, M.I.T., Aeronautics and Astronautics Department, June 2008.

Figure Captions

Figure 1: (Color online) Notional concept of experimental laboratory testbed emulator in which lasercom tracking schemes can be tested in a realistic environment that includes relevant impairments. The testbed includes both aircraft and spacecraft lasercom pointing, acquisition, and tracking functions. The full-duplex terminals interface through an emulated environment that introduces the impairments shown.

Figure 2: (Color online) Side and top view of the density flow field around a 400-mm (16-in) diameter hyper-hemispherical dome on an aircraft fuselage. Altitude: 29 kft; airspeed: Mach 0.7; units of scale: $\mathrm{lbm/ft^3}$.

Figure 3: Definitions for azimuth and elevation look angles. Curved arrows indicate positive angles.

Figure 4: (Color online) Plots from an experimental acquisition showing both power-level measurements for different sensors and state values for the spacecraft terminal (a) and aircraft terminal (b). The bottom plot (c) shows fiber-coupled receiver power for both terminals.

Figure 5: Bullseye plot used to display results. Boldface-type angles outside perimeter of circle indicate azimuth look angles; boldface, italicized-type angles inside the top octant define elevation look angles. Thus, each octant is divided into three regions that define different look angles; the central circle corresponds to the zenith look angle ($\boldsymbol{90^o}$ elevation). Grayed regions indicate cases where impairments prevented the link from acquiring. All angles are with respect to the aircraft.

Figure 6: (Color online) Differences [dB] in mean fiber-coupled power between tracking algorithms. Positive values indicate centroid tracking preferred, and negative values indicate peak tracking preferred. Regions marked with "X" represent look angles with unstable links.

Figure 7: (Color online) Differences [dB] in mean FPA peak-pixel power between tracking algorithms. Positive values indicate centroid tracking preferred, and negative values indicate peak tracking preferred. Regions marked with "X" represent look angles with unstable links.

Figure 8: (Color online) Differences [dB] in mean on-aperture power density between tracking algorithms. Positive values indicate centroid tracking preferred, and negative values indicate peak tracking preferred. Regions marked with "X" represent look angles with unstable links.

Figure 9: (Color online) Aircraft FPA azimuth and elevation error signals for peak and centroid tracking algorithms at 90°/20° (azimuth/elevation). The raw signals for each algorithm appear different from each other as expected. However, the traces closely resemble each other after applying 100-Hz, low-pass filtering representing the tracking-control-loop bandwidth.

Table Captions

Table 1: (Color online) Z test statistic scores between centroid algorithm (positive values) and peak algorithm (negative values) tracking. Significant scores ($|Z| > 2.58$) are tinted (colored red for centroid and blue for peak in online version). Entries marked ' – ' indicate that the impairments prevented the link from achieving stable performance, meaning useful data was not obtained at those look angles.

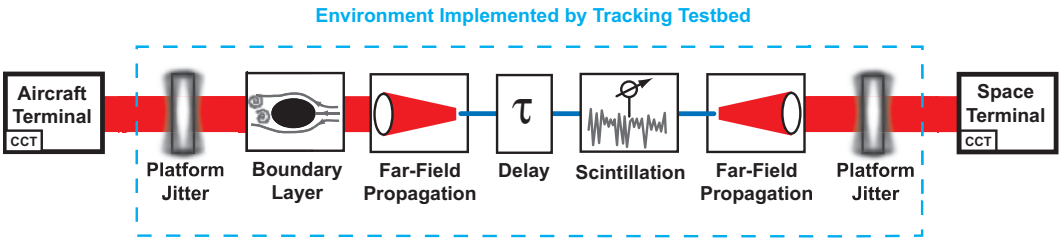

Fig. 1. (Color online) Notional concept of experimental laboratory testbed emulator in which lasercom tracking schemes can be tested in a realistic environment that includes relevant impairments. The testbed includes both aircraft and spacecraft lasercom pointing, acquisition, and tracking functions. The full-duplex terminals interface through an emulated environment that introduces the impairments shown.

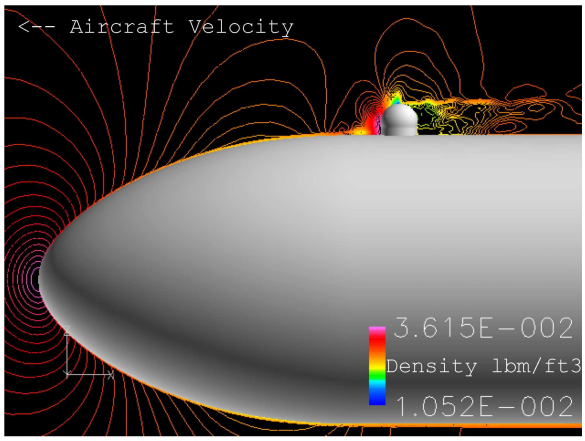

(a) Side View

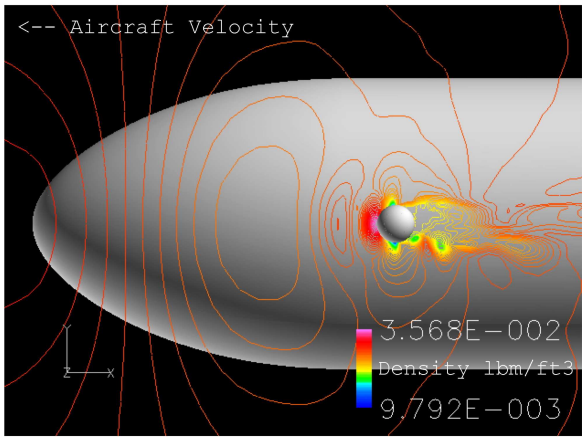

(b) Top View

Fig. 2. (Color online) Side and top view of the density flow field around a 400-mm (16-in) diameter hyper-hemispherical dome on an aircraft fuselage. Altitude: 29 kft; airspeed: Mach 0.7; units of scale: lbm/ft^3.

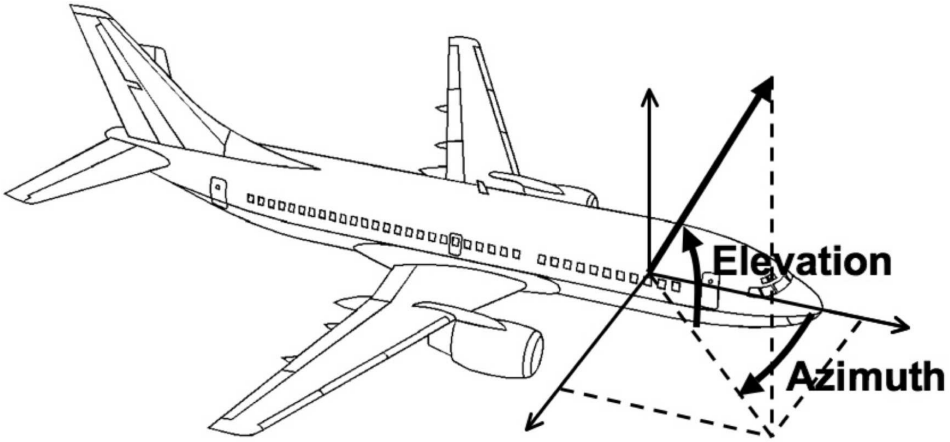

Fig. 3. Definitions for azimuth and elevation look angles. Curved arrows indicate positive angles.

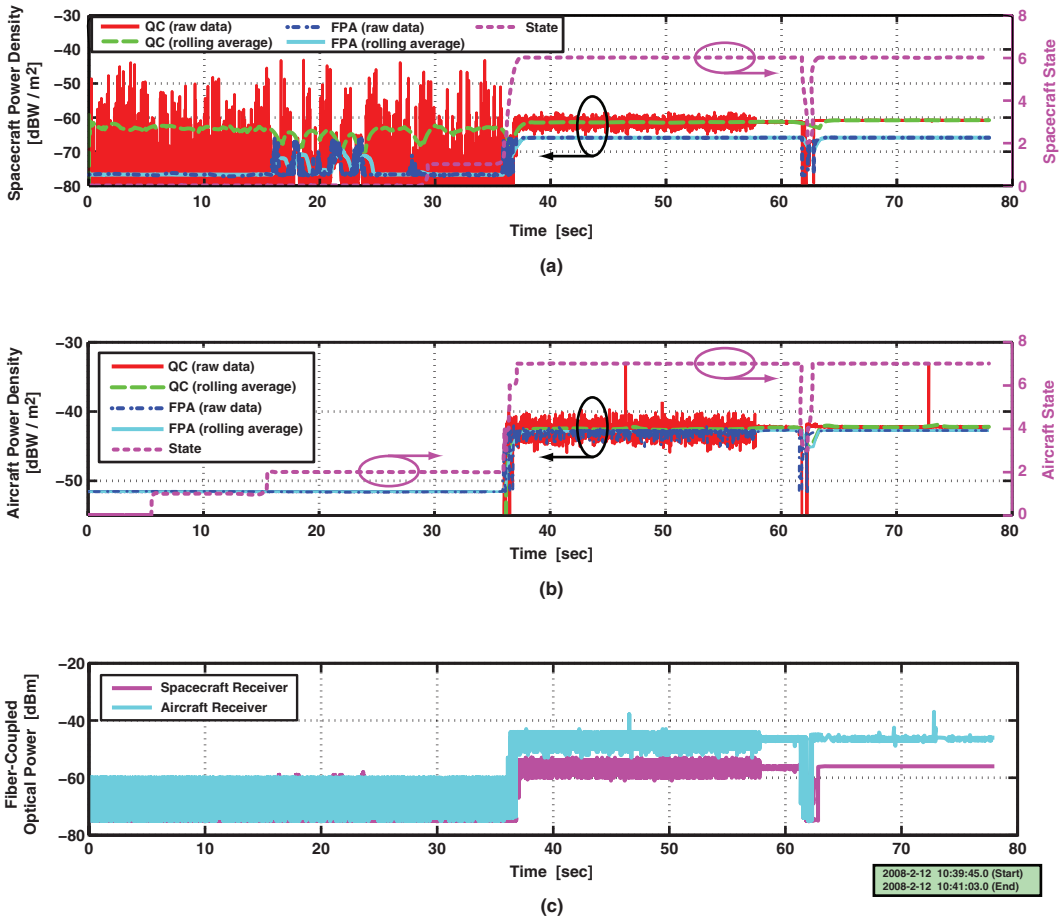

Fig. 4. (Color online) Plots from an experimental acquisition showing both power-level measurements for different sensors and state values for the spacecraft terminal (a) and aircraft terminal (b). The bottom plot (c) shows fiber-coupled receiver power for both terminals.

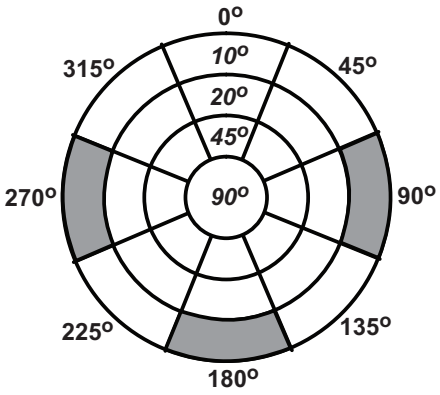

Fig. 5. Bullseye plot used to display results. Boldface-type angles outside perimeter of circle indicate azimuth look angles; boldface, italicized-type angles inside the top octant define elevation look angles. Thus, each octant is divided into three regions that define different look angles; the central circle corresponds to the zenith look angle (***90***^{o} elevation). Grayed regions indicate cases where impairments prevented the link from acquiring. All angles are with respect to the aircraft.

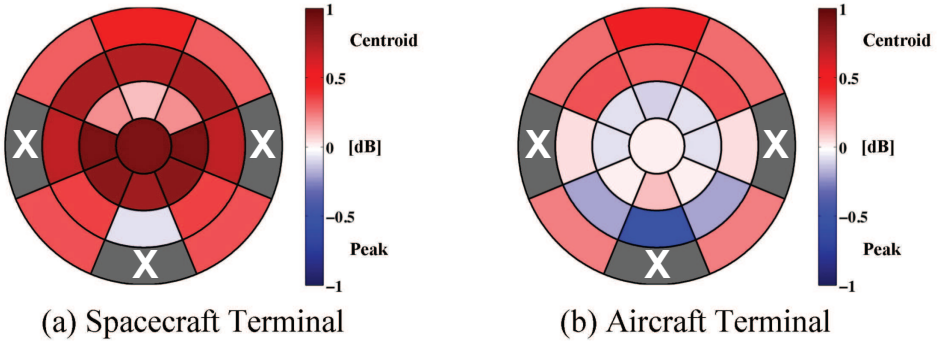

(a) Spacecraft Terminal (b) Aircraft Terminal

Fig. 6. (Color online) Differences [dB] in mean fiber-coupled power between tracking algorithms. Positive values indicate centroid tracking preferred, and negative values indicate peak tracking preferred. Regions marked with "X" represent look angles with unstable links.

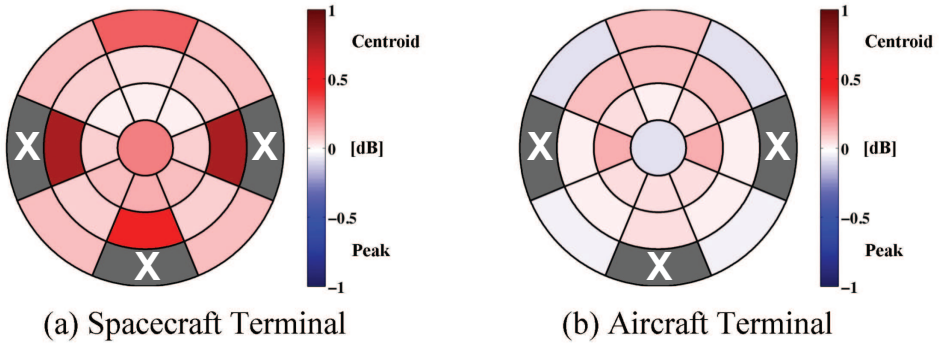

Fig. 7. (Color online) Differences [dB] in mean FPA peak-pixel power between tracking algorithms. Positive values indicate centroid tracking preferred, and negative values indicate peak tracking preferred. Regions marked with "X" represent look angles with unstable links.

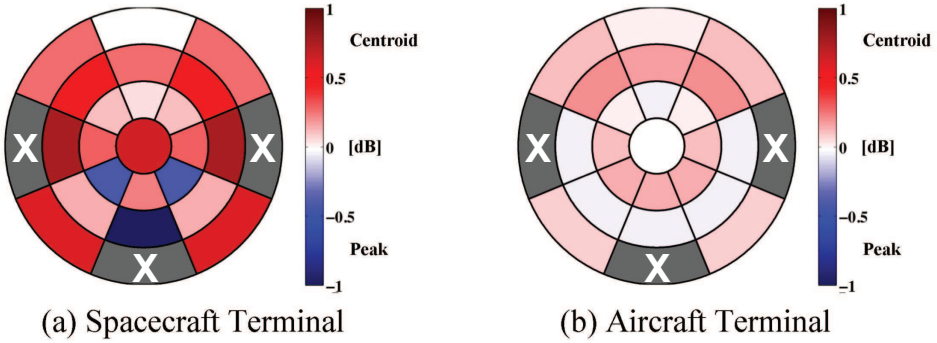

(a) Spacecraft Terminal (b) Aircraft Terminal

Fig. 8. (Color online) Differences [dB] in mean on-aperture power density between tracking algorithms. Positive values indicate centroid tracking preferred, and negative values indicate peak tracking preferred. Regions marked with "X" represent look angles with unstable links.

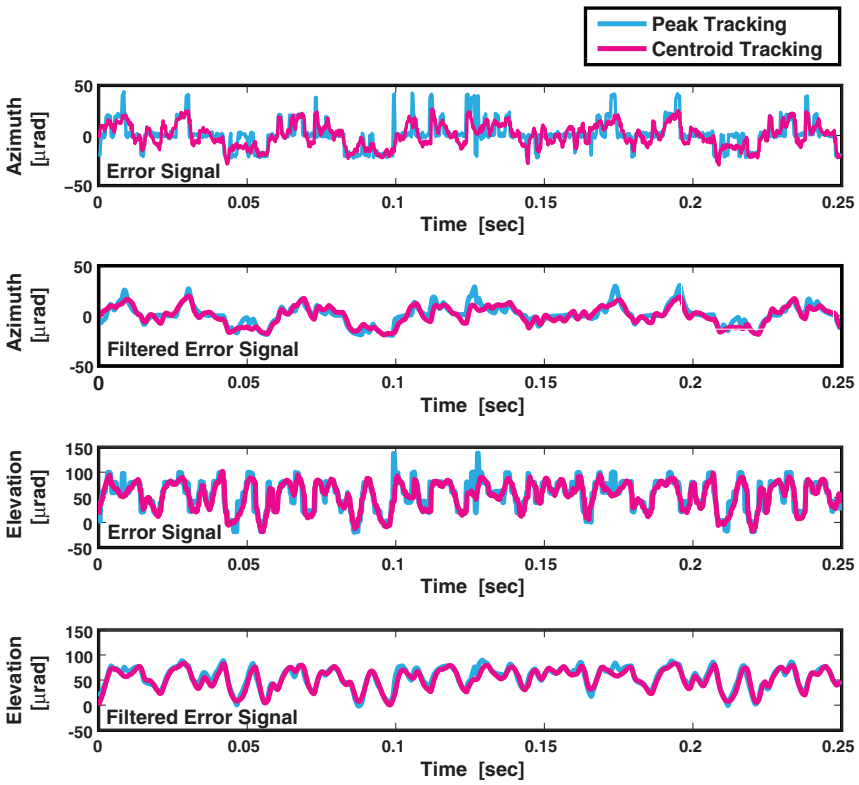

Fig. 9. (Color online) Aircraft FPA azimuth and elevation error signals for peak and centroid tracking algorithms at 90°/20° (azimuth/elevation). The raw signals for each algorithm appear different from each other as expected. However, the traces closely resemble each other after applying 100-Hz, low-pass filtering representing the tracking-control-loop bandwidth.

Table 1. (Color online) Z test statistic scores between centroid algorithm (positive values) and peak algorithm (negative values) tracking. Significant scores ($|Z| > 2.58$) are tinted (colored red for centroid and blue for peak in online version). Entries marked ' – ' indicate that the impairments prevented the link from achieving stable performance, meaning useful data was not obtained at those look angles.

Test Case	Azimuth (deg)	Elevation (deg)	Spacecraft Terminal Power			Aircraft Terminal Power		
			Aperture	FPA	Fiber	Aperture	FPA	Fiber
1.1	0	45	1.74	-1.16	3.36	-1.44	0.03	-3.68
1.2	45	45	3.35	3.71	7.11	0.44	3.64	-3.28
1.3	90	45	2.47	2.41	16.44	4.05	5.20	-1.54
1.4	135	45	-0.66	4.44	15.04	5.11	1.69	0.39
1.5	180	45	3.48	6.16	15.16	4.78	2.40	2.16
1.6	0	90	2.23	4.81	13.20	-0.37	-2.16	0.25
2.1	0	20	4.10	6.22	12.74	2.66	3.56	4.92
2.2	45	20	7.75	8.31	13.64	3.65	4.65	5.65
2.3	90	20	8.56	14.33	7.85	-1.14	0.34	0.59
2.4	135	20	1.88	4.46	5.75	-0.97	0.86	-3.28
2.5	180	20	-2.67	5.35	-0.90	-0.81	0.84	-4.19
3.1	0	10	-0.14	6.11	4.32	0.38	2.16	4.76
3.2	45	10	2.14	3.44	3.16	0.98	-1.32	2.31
3.3	90	10	–	–	–	–	–	–
3.4	135	10	4.90	3.71	3.45	0.70	-0.92	2.03
3.5	180	10	–	–	–	–	–	–